

Setting upper limits on the strength of periodic gravitational waves
using the first science data from the GEO 600 and LIGO detectors

B. Abbott,¹³ R. Abbott,¹³ R. Adhikari,¹⁴ B. Allen,³⁹ R. Amin,³⁴ S. B. Anderson,¹³ W. G. Anderson,²⁹ M. Araya,¹³
H. Armandula,¹³ F. Asiri,^{13, a} P. Aufmuth,³¹ C. Aulbert,¹ S. Babak,⁷ R. Balasubramanian,⁷ S. Ballmer,¹⁴
B. C. Barish,¹³ D. Barker,¹⁵ C. Barker-Patton,¹⁵ M. Barnes,¹³ B. Barr,³⁵ M. A. Barton,¹³ K. Bayer,¹⁴
R. Beausoleil,^{26, b} K. Belczynski,²³ R. Bennett,^{35, c} S. J. Berukoff,^{1, d} J. Betzwieser,¹⁴ B. Bhawal,¹³ G. Billingsley,¹³
E. Black,¹³ K. Blackburn,¹³ B. Bland-Weaver,¹⁵ B. Bochner,^{14, e} L. Bogue,¹³ R. Bork,¹³ S. Bose,⁴⁰ P. R. Brady,³⁹
J. E. Brau,³⁷ D. A. Brown,³⁹ S. Brozek,^{31, f} A. Bullington,²⁶ A. Buonanno,^{6, g} R. Burgess,¹⁴ D. Busby,¹³
W. E. Butler,³⁸ R. L. Byer,²⁶ L. Cadonati,¹⁴ G. Cagnoli,³⁵ J. B. Camp,²¹ C. A. Cantley,³⁵ L. Cardenas,¹³
K. Carter,¹⁶ M. M. Casey,³⁵ J. Castiglione,³⁴ A. Chandler,¹³ J. Chapsky,^{13, h} P. Charlton,¹³ S. Chatterji,¹⁴
Y. Chen,⁶ V. Chickarmane,¹⁷ D. Chin,³⁶ N. Christensen,⁸ D. Churches,⁷ C. Colacino,^{31, 2} R. Coldwell,³⁴
M. Coles,^{16, i} D. Cook,¹⁵ T. Corbitt,¹⁴ D. Coyne,¹³ J. D. E. Creighton,³⁹ T. D. Creighton,¹³ D. R. M. Crooks,³⁵
P. Csatorday,¹⁴ B. J. Cusack,³ C. Cutler,¹ E. D'Ambrosio,¹³ K. Danzmann,^{31, 2, 20} R. Davies,⁷ E. Daw,^{17, j}
D. DeBra,²⁶ T. Delker,^{34, k} R. DeSalvo,¹³ S. Dhurandar,¹² M. Díaz,²⁹ H. Ding,¹³ R. W. P. Drever,⁴ R. J. Dupuis,³⁵
C. Ebeling,⁸ J. Edlund,¹³ P. Ehrens,¹³ E. J. Elliffe,³⁵ T. Etzel,¹³ M. Evans,¹³ T. Evans,¹⁶ C. Fallnich,³¹
D. Farnham,¹³ M. M. Fejer,²⁶ M. Fine,¹³ L. S. Finn,²⁸ É. Flanagan,⁹ A. Freise,^{2, 1} R. Frey,³⁷ P. Fritschel,¹⁴
V. Frolov,¹⁶ M. Fyffe,¹⁶ K. S. Ganezer,⁵ J. A. Giaime,¹⁷ A. Gillespie,^{13, m} K. Goda,¹⁴ G. González,¹⁷ S. Goßler,³¹
P. Grandclément,²³ A. Grant,³⁵ C. Gray,¹⁵ A. M. Gretarsson,¹⁶ D. Grimmer,¹³ H. Grote,² S. Grunewald,¹
M. Guenther,¹⁵ E. Gustafson,^{26, n} R. Gustafson,³⁶ W. O. Hamilton,¹⁷ M. Hammond,¹⁶ J. Hanson,¹⁶ C. Hardham,²⁶
G. Harry,¹⁴ A. Hartunian,¹³ J. Heefner,¹³ Y. Hefetz,¹⁴ G. Heinzl,² I. S. Heng,³¹ M. Hennessy,²⁶ N. Hepler,²⁸
A. Heptonstall,³⁵ M. Heurs,³¹ M. Hewitson,³⁵ N. Hindman,¹⁵ P. Hoang,¹³ J. Hough,³⁵ M. Hrynevych,^{13, o} W. Hua,²⁶
R. Ingley,³³ M. Ito,³⁷ Y. Itoh,¹ A. Ivanov,¹³ O. Jennrich,^{35, p} W. W. Johnson,¹⁷ W. Johnston,²⁹ L. Jones,¹³
D. Jungwirth,^{13, q} V. Kalogera,²³ E. Katsavounidis,¹⁴ K. Kawabe,^{20, 2} S. Kawamura,²² W. Kells,¹³ J. Kern,¹⁶
A. Khan,¹⁶ S. Killbourn,³⁵ C. J. Killow,³⁵ C. Kim,²³ C. King,¹³ P. King,¹³ S. Klimentenko,³⁴ P. Kloevekor,²
S. Koranda,³⁹ K. Kötter,³¹ J. Kovalik,¹⁶ D. Kozak,¹³ B. Krishnan,¹ M. Landry,¹⁵ J. Langdale,¹⁶ B. Lantz,²⁶
R. Lawrence,¹⁴ A. Lazzarini,¹³ M. Lei,¹³ V. Leonhardt,³¹ I. Leonor,³⁷ K. Libbrecht,¹³ P. Lindquist,¹³ S. Liu,¹³
J. Logan,^{13, r} M. Lormand,¹⁶ M. Lubinski,¹⁵ H. Lück,^{31, 2} T. T. Lyons,^{13, r} B. Machenschalk,¹ M. MacInnis,¹⁴
M. Mageswaran,¹³ K. Mailand,¹³ W. Majid,^{13, h} M. Malec,³¹ F. Mann,¹³ A. Marin,^{14, s} S. Márka,¹³ E. Maros,¹³
J. Mason,^{13, t} K. Mason,¹⁴ O. Matherny,¹⁵ L. Matone,¹⁵ N. Mavalvala,¹⁴ R. McCarthy,¹⁵ D. E. McClelland,³
M. McHugh,¹⁹ P. McNamara,^{35, u} G. Mendell,¹⁵ S. Meshkov,¹³ C. Messenger,³³ G. Mitselmakher,³⁴
R. Mittleman,¹⁴ O. Miyakawa,¹³ S. Miyoki,^{13, v} S. Mohanty,¹ G. Moreno,¹⁵ K. Mossavi,² B. Mours,^{13, w}
G. Mueller,³⁴ S. Mukherjee,¹ J. Myers,¹⁵ S. Nagano,² T. Nash,¹⁰ H. Naundorf,¹ R. Nayak,¹² G. Newton,³⁵
F. Nocera,¹³ P. Nutzman,²³ T. Olson,²⁴ B. O'Reilly,¹⁶ D. J. Ottaway,¹⁴ A. Ottewill,^{39, x} D. Ouimette,^{13, q}
H. Overmier,¹⁶ B. J. Owen,²⁸ M. A. Papa,¹ C. Parameswariah,¹⁶ V. Parameswariah,¹⁵ M. Pedraza,¹³
S. Penn,¹¹ M. Pitkin,³⁵ M. Plissi,³⁵ M. Pratt,¹⁴ V. Quetschke,³¹ F. Raab,¹⁵ H. Radkins,¹⁵ R. Rahkola,³⁷
M. Rakhmanov,³⁴ S. R. Rao,¹³ D. Redding,^{13, h} M. W. Regehr,^{13, h} T. Regimbau,¹⁴ K. T. Reilly,¹³
K. Reithmaier,¹³ D. H. Reitze,³⁴ S. Richman,^{14, y} R. Riesen,¹⁶ K. Riles,³⁶ A. Rizzi,^{16, z} D. I. Robertson,³⁵
N. A. Robertson,^{35, 26} L. Robison,¹³ S. Roddy,¹⁶ J. Rollins,¹⁴ J. D. Romano,²⁹ J. Romie,¹³ H. Rong,^{34, m}
D. Rose,¹³ E. Rothhoff,²⁸ S. Rowan,³⁵ A. Rüdiger,^{20, 2} P. Russell,¹³ K. Ryan,¹⁵ I. Salzman,¹³ G. H. Sanders,¹³
V. Sannibale,¹³ B. Sathyaprakash,⁷ P. R. Saulson,²⁷ R. Savage,¹⁵ A. Sazonov,³⁴ R. Schilling,^{20, 2} K. Schlaufman,²⁸
V. Schmidt,^{13, aa} R. Schofield,³⁷ M. Schrempel,^{31, bb} B. F. Schutz,^{1, 7} P. Schwinberg,¹⁵ S. M. Scott,³ A. C. Searle,³
B. Sears,¹³ S. Seel,¹³ A. S. Sengupta,¹² C. A. Shapiro,^{28, cc} P. Shawhan,¹³ D. H. Shoemaker,¹⁴ Q. Z. Shu,^{34, dd}
A. Sibley,¹⁶ X. Siemens,³⁹ L. Sievers,^{13, h} D. Sigg,¹⁵ A. M. Sintes,^{1, 32} K. Skeldon,³⁵ J. R. Smith,² M. Smith,¹⁴
M. R. Smith,¹³ P. Sneddon,³⁵ R. Spero,^{13, h} G. Stapfer,¹⁶ K. A. Strain,³⁵ D. Strom,³⁷ A. Stuver,²⁸
T. Summerscales,²⁸ M. C. Sumner,¹³ P. J. Sutton,²⁸ J. Sylvestre,¹³ A. Takamori,¹³ D. B. Tanner,³⁴ H. Tariq,¹³
I. Taylor,⁷ R. Taylor,¹³ K. S. Thorne,⁶ M. Tibbits,²⁸ S. Tilav,^{13, ee} M. Tinto,^{4, h} C. Torres,²⁹ C. Torrie,^{13, 35}
S. Traeger,^{31, ff} G. Traylor,¹⁶ W. Tyler,¹³ D. Ugolini,³⁰ M. Vallisneri,^{6, h} M. van Putten,¹⁴ S. Vass,¹³ A. Vecchio,³³
C. Vorvick,¹⁵ L. Wallace,¹³ H. Walther,²⁰ H. Ward,³⁵ B. Ware,^{13, h} K. Watts,¹⁶ D. Webber,¹³ A. Weidner,^{20, 2}
U. Weiland,³¹ A. Weinstein,¹³ R. Weiss,¹⁴ H. Welling,³¹ L. Wen,¹³ S. Wen,¹⁷ J. T. Whelan,¹⁹ S. E. Whitcomb,¹³
B. F. Whiting,³⁴ P. A. Willems,¹³ P. R. Williams,^{1, gg} R. Williams,⁴ B. Willke,^{31, 2} A. Wilson,¹³ B. J. Winjum,^{28, d}
W. Winkler,^{20, 2} S. Wise,³⁴ A. G. Wiseman,³⁹ G. Woan,³⁵ R. Wooley,¹⁶ J. Worden,¹⁵ I. Yakushin,¹⁶
H. Yamamoto,¹³ S. Yoshida,²⁵ I. Zawischa,^{31, hh} L. Zhang,¹³ N. Zotov,¹⁸ M. Zucker,¹⁶ and J. Zweizig¹³

(The LIGO Scientific Collaboration, <http://www.ligo.org>)

- ¹Albert Einstein Institut für Gravitationsphysik, D-14476 Golm, Germany
²Albert Einstein Institut für Gravitationsphysik, D-30157 Hannover, Germany
³Australian National University, Canberra, 0200, Australia
⁴California Institute of Technology, Pasadena, CA 91125, USA
⁵California State University Dominguez Hills, Carson, CA 90747, USA
⁶Caltech-CaRT, Pasadena, CA 91125, USA
⁷Cardiff University, Cardiff, CF2 3YB, United Kingdom
⁸Carleton College, Northfield, MN 55057, USA
⁹Cornell University, Ithaca, NY 14853, USA
¹⁰Fermi National Accelerator Laboratory, Batavia, IL 60510, USA
¹¹Hobart and William Smith Colleges, Geneva, NY 14456, USA
¹²Inter-University Centre for Astronomy and Astrophysics, Pune - 411007, India
¹³LIGO - California Institute of Technology, Pasadena, CA 91125, USA
¹⁴LIGO - Massachusetts Institute of Technology, Cambridge, MA 02139, USA
¹⁵LIGO Hanford Observatory, Richland, WA 99352, USA
¹⁶LIGO Livingston Observatory, Livingston, LA 70754, USA
¹⁷Louisiana State University, Baton Rouge, LA 70803, USA
¹⁸Louisiana Tech University, Ruston, LA 71272, USA
¹⁹Loyola University, New Orleans, LA 70118, USA
²⁰Max Planck Institut für Quantenoptik, D-85748, Garching, Germany
²¹NASA/Goddard Space Flight Center, Greenbelt, MD 20771, USA
²²National Astronomical Observatory of Japan, Tokyo 181-8588, Japan
²³Northwestern University, Evanston, IL 60208, USA
²⁴Salish Kootenai College, Pablo, MT 59855, USA
²⁵Southeastern Louisiana University, Hammond, LA 70402, USA
²⁶Stanford University, Stanford, CA 94305, USA
²⁷Syracuse University, Syracuse, NY 13244, USA
²⁸The Pennsylvania State University, University Park, PA 16802, USA
²⁹The University of Texas at Brownsville and Texas Southmost College, Brownsville, TX 78520, USA
³⁰Trinity University, San Antonio, TX 78212, USA
³¹Universität Hannover, D-30167 Hannover, Germany
³²Universitat de les Illes Balears, E-07071 Palma de Mallorca, Spain
³³University of Birmingham, Birmingham, B15 2TT, United Kingdom
³⁴University of Florida, Gainesville, FL 32611, USA
³⁵University of Glasgow, Glasgow, G12 8QQ, United Kingdom
³⁶University of Michigan, Ann Arbor, MI 48109, USA
³⁷University of Oregon, Eugene, OR 97403, USA
³⁸University of Rochester, Rochester, NY 14627, USA
³⁹University of Wisconsin-Milwaukee, Milwaukee, WI 53201, USA
⁴⁰Washington State University, Pullman, WA 99164, USA
- (Dated: August 25, 2018)

Data collected by the GEO 600 and LIGO interferometric gravitational wave detectors during their first observational science run were searched for continuous gravitational waves from the pulsar J1939+2134 at twice its rotation frequency. Two independent analysis methods were used and are demonstrated in this paper: a frequency domain method and a time domain method. Both achieve consistent null results, placing new upper limits on the strength of the pulsar's gravitational wave emission. A model emission mechanism is used to interpret the limits as a constraint on the pulsar's equatorial ellipticity.

PACS numbers: 04.80.Nn, 95.55.Ym, 97.60.Gb, 07.05.Kf

^aCurrently at Stanford Linear Accelerator Center

^bCurrently at HP Laboratories

^cCurrently at Rutherford Appleton Laboratory

^dCurrently at University of California, Los Angeles

^eCurrently at Hofstra University

^fCurrently at Siemens AG

^gPermanent Address: GReCO, Institut d'Astrophysique de Paris

(CNRS)

^hCurrently at NASA Jet Propulsion Laboratory

ⁱCurrently at National Science Foundation

^jCurrently at University of Sheffield

^kCurrently at Ball Aerospace Corporation

^lCurrently at European Gravitational Observatory

^mCurrently at Intel Corp.

I. INTRODUCTION

This work presents methods to search for periodic gravitational waves generated by known pulsars, using data collected by interferometric gravitational wave detectors. To illustrate these methods, upper limits are placed on the strength of waves emitted by pulsar J1939+2134 at its expected 1284 Hz emission frequency during S1 [1]. S1 is the first observational science run of the LIGO [2, 3] and GEO [4, 5] detectors and it took place during 17 days between August 23 and September 9, 2002. The sensitivity of the searches presented here surpasses that of previous searches for gravitational waves from this source. However, measurements of the spin-down rate of the pulsar indicate that a detectable signal is very unlikely given the instrument performance for this data set: for these early observations the detectors were not operating at their eventual design sensitivities. Substantial improvements in detector noise have been achieved since the S1 observations, and further improvements are planned. We expect that the methods presented here will eventually enable the direct detection of periodic gravitational waves.

In Section II, we describe the configuration and calibration of the four LIGO and GEO interferometers and derive their expected sensitivities to periodic sources having known locations, frequencies and spindown rates. In Section III we consider proposed neutron star gravitational wave emission mechanisms, and introduce notation for describing the nearly monochromatic signals emitted by isolated neutron stars. Statistical properties of the data, analyses methods and results are presented in Section IV. These results are then summarized and compared in Section V. In Section V we also interpret the upper limits on the signal amplitude as a constraint on the ellipticity

of the pulsar and consider our results in the context of previous upper limits.

II. THE DETECTORS

Gravitational waves are a fundamental consequence of Einstein's General Theory of Relativity [6, 7], in which they represent perturbations of the spacetime metric which propagate at the speed of light. Gravitational waves produced by the acceleration of compact astrophysical objects may be detected by monitoring the motions they induce on freely-falling test bodies. The strength of these waves, called the *strain*, can be characterized by the fractional variation in the geodesic separation between these test bodies.

During the past decade, several scientific collaborations have constructed a new type of detector for gravitational waves. These large-scale interferometric detectors include the US Laser Interferometer Gravitational Wave Observatory (LIGO), located in Hanford, WA, and Livingston, LA, built by a Caltech-MIT collaboration [2, 3]; the GEO 600 detector near Hannover, Germany, built by a British-German collaboration [4, 5]; the VIRGO detector in Pisa, Italy, built by an Italian-French collaboration [8]; and the Japanese TAMA 300 detector in Tokyo [9]. In these detectors, the relative positions of suspended test masses are sensed interferometrically. A gravitational wave produces a time-varying differential displacement $\Delta L(t)$ in an interferometer that is proportional to its arm length L . The amplitude of the gravitational wave is described by the dimensionless strain $h(t) = \Delta L(t)/L$. For realistic periodic astrophysical sources we typically expect strain amplitudes smaller than 10^{-24} .

The following sections introduce the operating configurations of GEO 600 and LIGO detectors during the S1 run. The references provide more detailed descriptions of these detectors.

A. Instrument configurations

The GEO 600 detector comprises a 4-beam Michelson delay line system of arm length 600 m. The interferometer is illuminated by frequency-stabilized light from an injection-locked Nd:YAG laser. Before reaching the interferometer, the light is passed through two 8 m triangular mode-cleaning cavities. During S1 approximately 2 W of light was incident on the interferometer. A power recycling mirror of 1% transmission was installed to increase the effective laser power available for the measurement.

LIGO comprises three power-recycled Michelson interferometers with resonant Fabry-Perot cavity arms. A 4 km and a 2 km interferometer are collocated at the Hanford site and are designated H1 and H2 respectively, and a 4 km interferometer at the Livingston site is designated L1. Each interferometer employs a Nd:YAG laser stabilized using a monolithic reference cavity and a 12 m

ⁿCurrently at Lightconnect Inc.

^oCurrently at Keck Observatory

^pCurrently at ESA Science and Technology Center

^qCurrently at Raytheon Corporation

^rCurrently at Mission Research Corporation

^sCurrently at Harvard University

^tCurrently at Lockheed-Martin Corporation

^uCurrently at NASA Goddard Space Flight Center

^vPermanent Address: University of Tokyo, Institute for Cosmic Ray Research

^wCurrently at Laboratoire d'Annecy-le-Vieux de Physique des Particules

^xPermanent Address: University College Dublin

^yCurrently at Research Electro-Optics Inc.

^zCurrently at Institute of Advanced Physics, Baton Rouge, LA

^{aa}Currently at European Commission, DG Research, Brussels, Belgium

^{bb}Currently at Spectra Physics Corporation

^{cc}Currently at University of Chicago

^{dd}Currently at LightBit Corporation

^{ee}Currently at University of Delaware

^{ff}Currently at Carl Zeiss GmbH

^{gg}Currently at Shanghai Astronomical Observatory

^{hh}Currently at Laser Zentrum Hannover

mode-cleaning cavity.

In all four instruments the beam splitters, recycling mirrors and test masses are hung as pendulums from multilayer seismic isolation filters to isolate them from local forces. The masses and beam paths are housed in high vacuum enclosures to preclude optical scintillation and acoustic interference.

Sinusoidal calibration forces of known amplitude were applied to the test bodies throughout the observing run. These signals were recovered from the data stream and used to periodically update the scale factors linking recorded signal amplitude to strain. The principal calibration uncertainties arise from the imprecision in the electromechanical coupling coefficients of the force actuators. These were estimated by comparison with the known laser wavelength, by actuating a test mass between interference fringes. In the Hanford interferometers, the calibration was also verified against piezoelectric displacement transducers connected to the mirror support structures. For the S1 observations, the net amplitude uncertainty was estimated at $\pm 4\%$ for GEO, $\pm 10\%$ for each of the LIGO interferometers.

B. Expected sensitivity

We define the gravitational wave strength h_0 of a continuous signal from a given source as the maximum peak amplitude which could be received by an interferometer if the orientation of the pulsar and the detector were both optimal. Thus, h_0 depends on the intrinsic emission strength and on the source distance, but not on the inclination of the pulsar's spin axis or on the antenna pattern of the detector.

The calibrated interferometer strain output is a time series

$$s(t) = h(t) + n(t), \quad (2.1)$$

where $h(t)$ is the received signal, $n(t)$ is the detector noise and t is the time in the detector's frame.

The noise $n(t)$ is characterized by its single-sided power spectral density $S_n(f)$. Assuming this noise is Gaussian and taking some fixed observation time¹ T , we can compute the amplitude h_0 of a putative continuous signal which would be detected in, e.g., 90% of experimental trials if truly present, but would arise randomly from the noise background in only 1% of trials (what we call a 1% "false alarm rate" and a 10% "false dismissal rate").

If we fix a false alarm rate, it is clear that the lower the desired false dismissal rate the higher the signal needs to be. The detection statistic used in section IV C provides the lowest false dismissal rate for a given false alarm rate

¹ Here we presume that we know the position, frequency and spin-down parameters of the source and that T is between a few days and several months.

and signal strength and it is thus optimal in the Neyman-Pearson sense (see for example [10]). The amplitude of the average signal that we could detect in Gaussian stationary noise with a false alarm rate of 1% and a false dismissal rate of 10% using the detection statistic described in [11] is given by²

$$\langle h_0 \rangle = 11.4 \sqrt{S_n(f_s)/T}, \quad (2.2)$$

where f_s is the frequency of the signal³. The upper curves in Fig. 1 show $\langle h_0 \rangle$ for the LIGO and GEO detectors during S1. Observation times for respective interferometers are given in the figure. Because of ground motion, equipment failures and alignment drifts, the four interferometers were not always fully operational during the S1 run, thus the observation times vary from detector to detector.

The lower curves in Fig. 1 represent $\langle h_0 \rangle$ corresponding to the design sensitivity of the various detectors. An observation of $T = 1$ y was assumed.

The filled circles in Fig. 1 show the constraints that measurements of spin-down rates of known pulsars place on the expected gravitational wave signal, under the assumption that the pulsars are rigid rotators with a moment of inertia of 10^{45} g cm² and *that all the observed spin-down rate is due to the emission of gravitational waves*.

As shown in Fig. 1, under the above assumptions no detection is expected for any known pulsar at the sensitivity achieved during the S1 run. Furthermore, many known pulsars are rotating too slowly to be detected by the initial ground-based interferometers. However, the number of millisecond pulsars observed in this band continues to increase with new radio surveys, and the known targets plotted here constitute a highly selected sample. Future searches for previously undiscovered rotating neutron stars using the methods presented here will sample a different and potentially much larger subset of the total population.

III. PERIODIC GRAVITATIONAL WAVES

A. Expected emission by neutron stars

The strongest argument that some neutron stars (NSs) *are* emitting gravitational waves (GWs) with amplitude

² The average is over different positions, inclinations and polarizations of the source.

³ This differs from [12] for three reasons: 1) the h_0 used here is twice that defined in [12], 2) we use a different statistic for this detection problem (a chi-square distribution with 4 degrees of freedom) and 3) we have specified a false dismissal rate of 10% whereas the derivation in [12] has an implicit false dismissal rate of about 50%. If we use this false dismissal rate and the \mathcal{F} statistic we get $\langle h_0 \rangle = 7.6 \sqrt{S_n(f_s)/T}$.

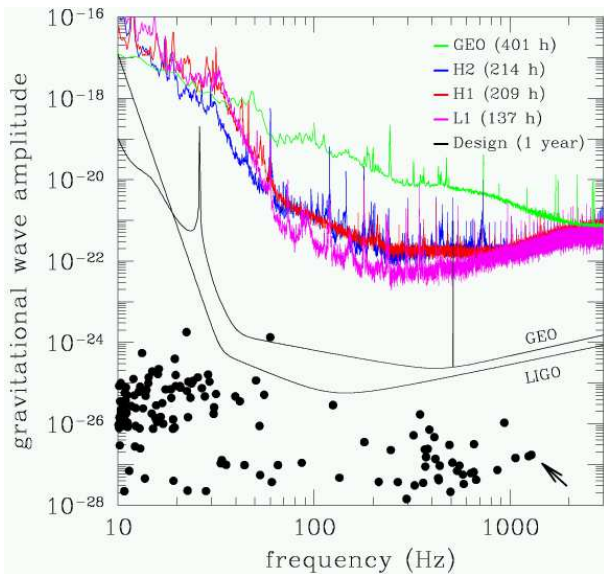


FIG. 1: Upper curves: characteristic amplitude $\langle h_0 \rangle$ of a known monochromatic signal detectable with a 1% false alarm rate and a 10% false dismissal rate by the GEO and LIGO detectors at the S1 sensitivity and with an observation time equal to the up-time of the detectors during S1 (GEO: 401 h, L1: 137 h, H1: 209 h, H2: 214 h). Lower curves: $\langle h_0 \rangle$ for the design sensitivities of the detectors for an assumed 1 y observation time. Filled circles: upper limit on $\langle h_0 \rangle$ from measured spin-down rate of known radio pulsars assuming a moment of inertia of 10^{45} g cm^2 . These upper limits were derived under the assumption that all the measured loss of angular momentum of the star is due to the emission of gravitational waves, neglecting spin-down contribution from electromagnetic and particle emission. The arrow points to the filled circle representing pulsar J1939+2134.

detectable by Advanced LIGO [13], $h_0 \gtrsim 10^{-27} - 10^{-26}$, is due to Bildsten [14, 15]. He noted that the inferred rotation frequencies of low-mass X-ray binaries (LMXBs) are all clustered in the range $f_r \sim 270 - 620 \text{ Hz}$ (an inference strengthened by the recent observations of [16, 17]), whereas *a priori* there should be no cut-off in f_r , up to the (estimated) NS break-up frequency of $\sim 1.5 \text{ kHz}$. Updating a suggestion by Wagoner [18, 19], Bildsten proposed that LMXBs have reached an equilibrium where spin-up due to accretion is balanced by spin-down from GW emission. Since the GW spin-down torque scales like f_r^5 , a wide range of accretion rates then leads to a rather narrow range of equilibrium rotation rates, as observed.

Millisecond pulsars (MSPs) are generally believed to be recycled pulsars: old pulsars that were spun up by accretion during an LMXB phase ([20, 21]). The rotation rates of MSPs also show a high-frequency cut-off [15]; the fastest (PSR J1939+2134) has $f_r = 642 \text{ Hz}$. If the GWs that arrest the spin-up of accreting NSs continue to be emitted in the MSP phase (e.g., because of some persistent deformation of the NS shape away from axisymmetry), then they could also account for the observed spin-down of MSPs. In this case, the GW amplitudes

of MSPs would in fact be (very close to) the ‘spin-down upper limits’ shown in Fig. 1. (Note that the MSP’s spin-down rate is generally attributed entirely to the pulsar’s magnetic field; indeed, pulsar magnetic fields are typically inferred this way. However, there appears to be no strong evidence supporting this inference.)

We now turn to the possible physical mechanisms responsible for periodic GWs in this frequency range. The main possibilities that have been considered are 1) NS spin precession, 2) an excited NS oscillation mode (mostly likely the r-mode), and 3) small distortions of the NS shape away from axisymmetry. At present the third mechanism (small ellipticity) seems the most plausible source of detectable GWs, and in this paper we set upper limits for this particular mechanism (the three mechanisms predict three different GW frequencies for the same observed rotation frequency). However, we begin by briefly commenting on the other two possibilities.

A NS precesses (or ‘wobbles’) when its angular momentum \mathbf{J} is not aligned with any principal axis of its inertia tensor. A wobbling NS emits GWs at the inertial-frame precession frequency, which is very nearly the rotation frequency, f_r . While large-amplitude wobble could plausibly produce GW amplitudes $h_0 \sim 10^{-27}$ over short timescales, the problem with this mechanism is that dissipation should damp NS wobble quickly [22]; while this dissipation timescale is quite uncertain (it is perhaps of order a year for a MSP), it is almost certainly orders of magnitude shorter than typical lifetimes of MSPs. So unless some mechanism is found that regularly re-excites large-amplitude wobble, it is unlikely that any nearby MSP would be wobbling. Moreover, most MSPs have highly stable pulse shapes, and typically appear *not* to be wobbling substantially. In particular, the single-pulse characteristics of PSR J1939+2134 have been observed to be extremely stable with no pulse-to-pulse variation except for occasional giant pulses [23]. It has been verified through radio observations that PSR J1939+2134 continued to spin according to a simple spin-down model during S1 [24].

R-modes (modes driven by Coriolis forces) have been a source of excitement among GW theorists since 1998, when Andersson [25] and Friedman and Morsink [26] showed that they should be unstable due to gravitational back-reaction (the Chandrasekhar-Friedman-Schutz instability). Nonlinear mode-mode coupling is predicted to saturate the growth of r-modes at dimensionless amplitude $\alpha \lesssim 10^{-3} (f_r/\text{kHz})^{5/2}$ [27]. This implies r-mode radiation from nascent NSs in extragalactic supernovae will not be detectable, but r-mode GWs from old, recycled Galactic NSs could still be detectable by Advanced LIGO. For example, GWs from an excited r-mode could balance accretion torque in accreting NSs, as in the Wagoner-Bildsten mechanism.

We now turn to GWs from small non-axisymmetries in the NS shape. If h_0 is the amplitude of the signal at the detector from an optimally oriented source, as described above, and if we assume that the emission mechanism is

due to deviations of the pulsar's shape from perfect axial symmetry, then

$$h_0 = \frac{4\pi^2 G}{c^4} \frac{I_{zz} f_s^2}{r} \epsilon, \quad (3.1)$$

where r is the distance to the NS, I_{zz} is its principal moment of inertia about the rotation axis, $\epsilon \equiv (I_{xx} - I_{yy})/I_{zz}$ is its ellipticity, and the gravitational wave signal frequency, f_s , is exactly twice the rotation frequency, f_r . G is Newton's constant, and c is the speed of light. This is the emission mechanism that we assume produces the gravitational wave signal that we are targeting.

One possible source of ellipticity is tiny 'hills' in the NS crust, which are supported by crustal shear stresses. In this case, the maximum ellipticity is set by the crustal breaking strain $\bar{\sigma}_{\max}$ [28]:

$$\epsilon_{\max} \approx 5 \times 10^{-8} (\bar{\sigma}_{\max}/10^{-3}). \quad (3.2)$$

The coefficient in Eq. 3.2 is low both because a NS's crust is rather thin (compared to the NS radius), and because the crust's shear modulus μ is small compared to the ambient pressure p : $\mu/p \sim 10^{-3} - 10^{-2}$. (If NSs have solid cores, as well as crusts, then much larger ellipticities would be possible.) For the LMXBs, Ushomirsky, Cutler & Bildsten [28] showed that lateral temperature variations in the crust of order 5%, or lateral composition variations of order 0.5% (in the charge-to-mass ratio), could build up NS ellipticities of order $10^{-8} - 10^{-7}$, but only if the crust's breaking strain is large enough to sustain such hills.

Strong internal magnetic fields are another possible source of NS ellipticity. Cutler [29] has argued that if a NS's interior magnetic field B has a toroidal topology (as expected if the B field was generated by strong differential rotation immediately after collapse), then dissipation tends to re-orient the symmetry axis of the toroidal B field perpendicular to the rotation axis, which is the ideal orientation for maximizing equatorial ellipticity. Toroidal B fields of order $10^{12} - 10^{13}$ G would lead to sufficient GW emission to halt the spin-up of LMXBs and account for the observed spin-down of MSPs.

B. The signal received from an isolated pulsar

A gravitational wave signal we detect from an isolated pulsar will be amplitude-modulated by the varying sensitivity of the detector as it rotates with the Earth (the detector's 'antenna pattern'). The detected strain has the form [11]

$$h(t) = F_+(t, \psi) h_0 \frac{1 + \cos^2 \iota}{2} \cos \Phi(t) + F_\times(t, \psi) h_0 \cos \iota \sin \Phi(t), \quad (3.3)$$

where ι is the angle between neutron star's spin direction \hat{s} and the propagation direction of the waves $\hat{\mathbf{k}}$, and $\Phi(t)$

right ascension (J2000)	19 ^h 39 ^m 38 ^s .560 210(2)
declination (J2000)	+21° 34 ^m 59 ^s .141 66(6)
RA proper motion	-0.130(8) mas yr ⁻¹
dec proper motion	-0.464(9) mas yr ⁻¹
period (1/ f_r)	0.001 557 806 468 819 794(2) s
period derivative	1.051 193(2) $\times 10^{-19}$ s s ⁻¹
epoch of period and position	MJDN 47 500

TABLE I: Parameters for the target pulsar of the analyses presented here, PSR J1939+2134 (also designated PSR B1937+21). Numbers in parentheses indicate uncertainty in the last digit.

is the phase evolution of the signal. $F_{+, \times}$ are the strain antenna patterns of the detector to the plus and cross polarizations and are bounded between -1 and 1. They depend on the orientation of the detector and the source, and on the polarization of the waves, described by the polarization angle ψ ⁴.

The signal will also be Doppler shifted by the orbital motion and rotation of the Earth. The resulting phase evolution of the received signal can be described by a truncated Taylor series as

$$\Phi(t) = \phi_0 + 2\pi[f_s(T - T_0) + \frac{1}{2}\dot{f}_s(T - T_0)^2 + \frac{1}{6}\ddot{f}_s(T - T_0)^3], \quad (3.4)$$

where

$$T = t + \delta t = t - \frac{\mathbf{r}_d \cdot \hat{\mathbf{k}}}{c} + \Delta_{E\odot} - \Delta_{S\odot}. \quad (3.5)$$

Here, T is the time of arrival of a signal at the solar system barycentre (SSB), ϕ_0 is the phase of the signal at fiducial time T_0 , \mathbf{r}_d is the position of the detector with respect to the SSB, and $\Delta_{E\odot}$ and $\Delta_{S\odot}$ are the solar system Einstein and Shapiro time delays respectively [30].

The timing routines used to compute the conversion between terrestrial and SSB time (Eq. 3.5) were checked by comparison with the widely-used radio astronomy timing package TEMPO [31]. This comparison (Figure 2) confirmed an accuracy of better than $\pm 4 \mu\text{s}$, thus ensuring no more than 0.01 radian phase mismatch between a putative signal and its template. This results in a negligible fractional signal-to-noise ratio loss, of order $\sim 10^{-4}$.

Table I shows the parameters of the pulsar that we have chosen to illustrate our analysis methods [34].

⁴ Following the conventions of [11], ψ is the angle (clockwise about $\hat{\mathbf{k}}$) from $\hat{\mathbf{z}} \times \hat{\mathbf{k}}$ to $\hat{\mathbf{k}} \times \hat{\mathbf{s}}$, where $\hat{\mathbf{z}}$ is directed to the North Celestial Pole. $\hat{\mathbf{k}} \times \hat{\mathbf{s}}$ is the x -axis of the wave frame – also called the waves' principal + polarization direction.

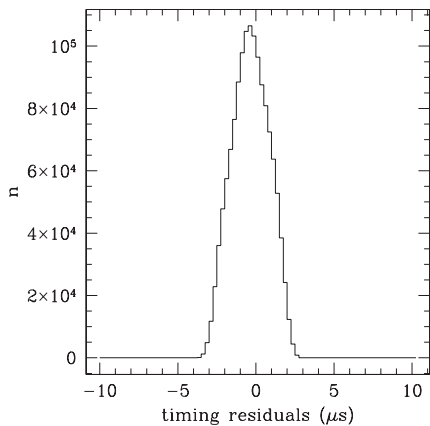


FIG. 2: Histogram of timing residuals between our barycentring routines and TEMPO, derived by comparing the phase evolution of test signals produced by the two software packages. 156 locations in the sky were chosen at random and the residuals calculated once an hour for the entire year 2002. The maximum timing error is $< 4 \mu\text{s}$.

IV. DATA ANALYSES

A. Introduction

Two independent search methods are presented here: i) a frequency domain method which can be employed for exploring large parameter space volumes and ii) a time domain method for targeted searches of systems with an arbitrary but known phase evolution.

Both approaches will be used to cast an upper limit on the amplitude of the periodic gravitational wave signal: a Bayesian approach for the time domain analysis and a frequentist approach for the frequency domain analysis. These approaches provide answers to two different questions and therefore should not be expected to result in the exact same numerical answer [32, 33]. The frequentist upper limit refers to the reliability of a procedure for identifying an interval that contains the true value of h_0 . In particular, the frequentist confidence level is the fraction of putative observations in which, in the presence of a signal at the level of the upper limit value identified by the actual measurement, $h_0^{95\%}$, the upper limit identified by the frequentist procedure would have been higher than $h_0^{95\%}$. The Bayesian upper limit, on the other hand, defines an interval in h_0 that, based on the observation made and on prior beliefs, includes the true value with 95% probability. The probability that we associate with the Bayesian upper limit characterizes the uncertainty in h_0 given the observation made. This is distinct from the reliability, evaluated over an ensemble of observations, of a procedure for identifying intervals.

All the software used for the analyses is part of the publicly available LSC Algorithm Library (LAL, [35]). This is a library that comprises roughly 700 functions specific to gravitational wave data analysis.

spin-down	$-8.663\,3(43) \times 10^{-14} \text{ Hz s}^{-1}$
f_s at start of GEO observation	1 283.856 487 705(5) Hz
f_s at start of L1 observation	1 283.856 487 692(5) Hz
f_s at start of H1 observation	1 283.856 487 687(5) Hz
f_s at start of H2 observation	1 283.856 487 682(5) Hz

TABLE II: Run parameters for PSR J1939+2134. The different emission frequencies correspond to the different initial epochs at which each of the searches began. Numbers in parentheses indicate the uncertainty in the last digit or digits.

B. Statistical characterization of the data

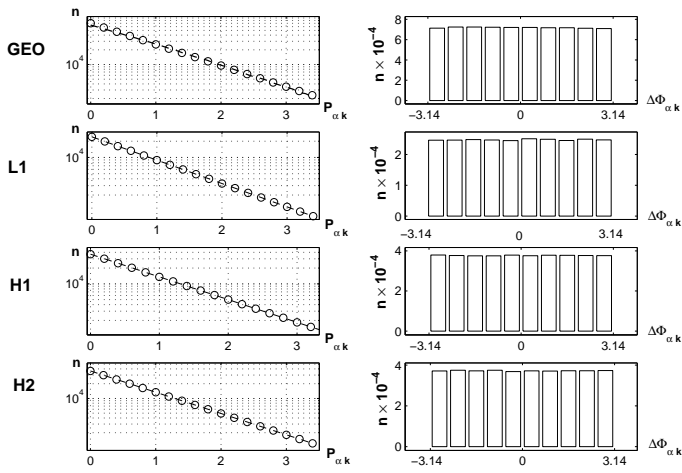
Due to the narrow frequency band in which the target signal has appreciable energy, it is most convenient to characterize the noise in the frequency domain. We divided the data into 60 s blocks and took the Fourier transform of each. The resulting set of Fourier transforms will be referred to as SFTs (Short time-baseline Fourier Transforms) and is described in more detail in IV C 1.

The frequency of the pulsar signal at the beginning of the observation for every detector is reported in Table II. Also reported is the value of the spin-down parameter expressed in units of Hz s^{-1} . We have studied the statistical properties of the data in a narrow frequency band (0.5 Hz) containing the emission frequency. This is the frequency search region, as well as the region used for estimating both the noise background and the detection efficiency. Fig. 3 summarizes our findings. Two types of distributions are plotted. The first column shows the distributions of bin power; for each SFT (labelled by α) and for every frequency bin (labelled by $1 \leq k \leq M$) in the band 1 283.75 to 1 284.25 Hz, we have computed the quantity

$$P_{\alpha k} = \frac{|\tilde{x}_{\alpha k}|^2}{\sum_k^M |\tilde{x}_{\alpha k}|^2 / M}, \quad (4.1)$$

where $\tilde{x}_{\alpha k}$ is the SFT datum at frequency index k of the α -th SFT, and have histogrammed these values. If the data are Gaussian and if the different frequency bins in every SFT are independent realizations of the same random process, then we expect the normalized power variable described above ($P_{\alpha k}$) to follow an exponential distribution with a mean and standard deviation of 1, as shown by the dashed line. The circles are the experimental points. The standard deviation of the measured distribution for GEO data is 0.95. The LIGO Livingston, Hanford 4 km and Hanford 2 km data are also shown in Fig. 3. The standard deviation of the $P_{\alpha k}$ for all of these is 0.97.

The plots in the second column of Fig. 3 show the distribution of phase differences between adjacent frequency bins. With the same notation as above, we have com-


 FIG. 3: Histograms of $P_{\alpha k}$ and of $\Delta\Phi_{\alpha k}$ for the four detectors.

puted the quantity

$$\Delta\Phi_{\alpha k} = \Phi_{\alpha k} - \Phi_{\alpha k-1}, \quad (4.2)$$

where $\Phi_{\alpha k}$ is the phase of the SFT datum at frequency index k of the α -th SFT and the difference is reduced to the range $[-\pi, \pi]$. $\Delta\Phi_{\alpha k}$ is therefore the distance in phase between data at adjacent frequency bins. If the data were from a purely random process we expect this distribution to be uniform between $-\pi$ and π , as observed.

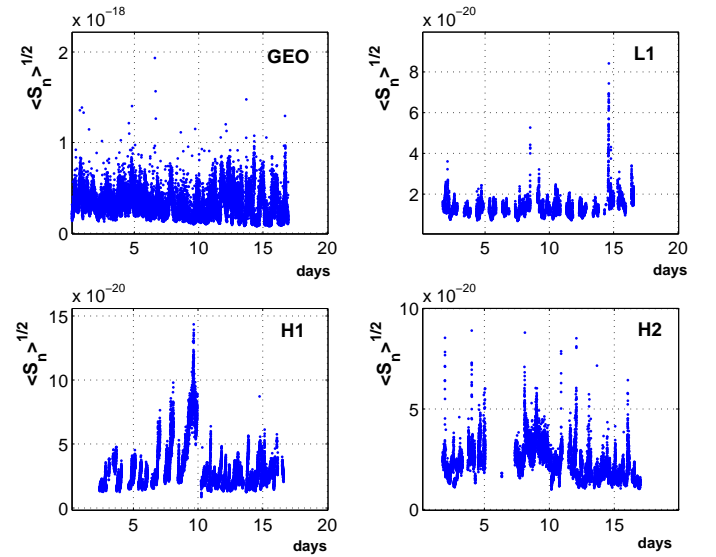
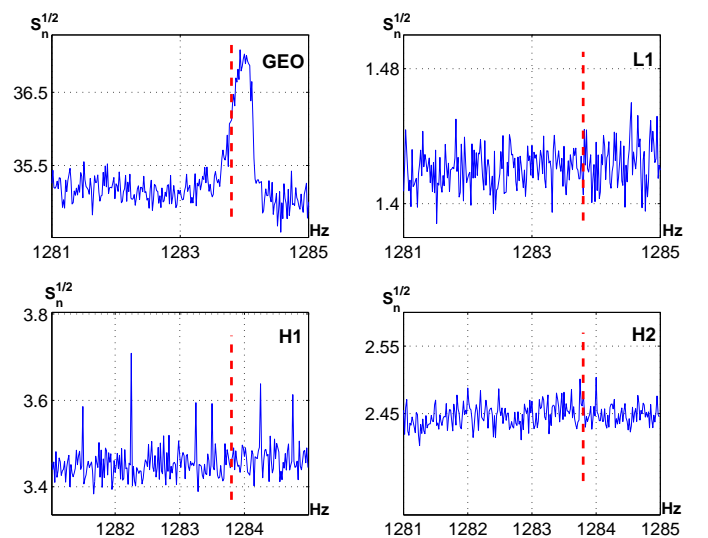
Fig. 4 shows the average value of $\sqrt{S_n}$ over a 1 Hz band from 1283.5 to 1284.5 Hz as a function of time in days for the entire S1 run starting from the beginning of S1 (15:00 UTC, August 23 2002). These plots monitor the stationarity of the noise in the band of interest over the course of the run.

Fig. 5 shows $\sqrt{S_n}$ as a function of frequency between 1281 and 1285 Hz. During S1 the received signal is expected to have a frequency 1283.8 Hz. This frequency is shown as a dashed vertical line. During the S1 observation time the Doppler modulation changed this signal frequency by no more than 0.03 Hz, two SFT frequency bins. For these plots S_n has been estimated by averaging the power in each frequency bin over the entire S1 run. A broad spectral feature is observed in the GEO data. This feature is 0.5 Hz wide, comparatively broad with respect to the expected Doppler shift of the target signal, and represents only a 10% perturbation in the local power spectral density.

C. The frequency domain technique

1. The Short time baseline Fourier Transforms

In principle the only constraint on the time baseline of the SFTs used in the frequency domain analysis is that the instantaneous frequency of a putative signal does not shift during the time baseline by more than half a frequency bin. For frequencies in the kiloHertz range this


 FIG. 4: The square root of the average value of S_n for all four interferometers over a band of 1 Hz starting at 1283.5 Hz versus time in days starting at the beginning of S1 (August 23 2002, 15:00 UTC).

 FIG. 5: $\sqrt{S_n}$ in a band of 4 Hz (starting at 1281 Hz) using the entire S1 data set analyzed from the four interferometers. The noise $\sqrt{S_n}$ is shown in units of $10^{-20} \text{ Hz}^{-1/2}$. The dashed vertical line indicates the expected frequency of the signal received from J1939+2134.

implies a maximum time baseline of order 30 min (having assumed an observation time of several months and a source declination roughly the same as the latitude of the detector). However, in practice, since we are also estimating the noise on the same time baseline, it is advisable for the time baseline to be short enough to follow the non-stationarities of the system. On the other hand, for the frequency-domain analysis, the computational time required to carry out a search increases linearly with the

number of Fourier transforms. Thus the shorter the time baseline, the higher the computational load. We have chosen for the S1 run a time baseline of 60s as a compromise between the two opposing needs.

Interruptions in interferometer operation broke each time series into segments separated by gaps representing invalid or contaminated data. Only valid data segments were included in the analysis. Each valid 60s data segment was filtered with a fifth-order Butterworth high-pass filter having a knee frequency of 100 Hz. Then, a nearly flat-top Tukey window function was applied to each data segment in the time domain. The window changes the value of less than 1% of the data in each 60s chunk. Each data segment was then Fast Fourier Transformed and written to an SFT file. These SFTs were computed once and then used repeatedly for different analyses.

2. The \mathcal{F} statistic

The detection statistic that we use is described in [11]. As in [11] we call this statistic \mathcal{F}^5 , though differences between our definition and that given in [11] are pointed out below.

The \mathcal{F} statistic derives from the method of maximum likelihood. The log likelihood function, $\ln \Lambda$, is, for Gaussian noise

$$\ln \Lambda = (s|h) - \frac{1}{2}(h|h), \quad (4.3)$$

where

$$(s|y) = 4\Re \int_0^\infty \frac{\tilde{s}(f)\tilde{y}^*(f)}{S_n(f)} df. \quad (4.4)$$

s is the calibrated detector output time series, h is the target signal (commonly referred to as the template), $\tilde{\cdot}$ is the Fourier transform operator, and $S_n(f)$ is the one-sided power spectral density of the noise. The \mathcal{F} statistic is the maximum value of $\ln \Lambda$ with respect to all the unknown signals parameters, given our data and a set of known template parameters. In fact, if some or all of the signal's parameters are unknown, it is standard practice to compute the likelihood for different template parameters and look for the highest values. The maximum of the likelihood function is the statistic of choice for matched filtering methods, and it is the optimal detection statistic as defined by the Neyman-Pearson criterion: lowest false dismissal rate at a fixed false alarm rate (see, for example, Section II B).

In our case the known parameters are the position of the source (α, δ angles on the celestial sphere), the emission frequency f_s and the first order spin-down parameter value \dot{f}_s . The unknown parameters are the orientation of the pulsar (angle ι), the polarization state of the wave (angle ψ), its initial phase ϕ_0 , and the wave's amplitude h_0 .

The core of the calculation of \mathcal{F} consists in computing integrals of the type given in Eq. 4.4, using templates for the two polarizations of the wave. The results are optimally combined as described in [11] except we consider a single frequency component signal. Also, we do not treat $S_n(f)$ as constant in time. Thus, while the method is defined in [11] in the context of stationary Gaussian noise, we adapt it so that it can be used even when the noise is nonstationary. The calculation is easily performed in the frequency domain since signal energy is concentrated in a narrow frequency band. Using the SFTs described in IV C 1 some approximations can be made to simplify the calculation and improve computational efficiency while still recovering most ($> 98\%$) of the signal power.

The method of computing \mathcal{F} was developed for a specific computational architecture: a cost-effective Beowulf cluster, which is an ensemble of loosely-coupled processors with simple network architecture. This becomes crucial when exploring very large parameter-space volumes for unknown sources using long observation periods, because the search depth and breadth are limited by computational resources. The S1 analyses described here were carried out using Condor [36] on the Merlin and Medusa clusters at the AEI and UWM respectively [37, 38]. Each cluster has 300 independent CPUs.

As a point of reference we note that it takes of order of a few seconds of CPU time on a 1.8 GHz-class CPU to determine the \mathcal{F} statistic for a single template with ~ 16 d of observation time.

3. Setting an upper limit on h_0

The outcome \mathcal{F}^* of a specific targeted search represents the optimal detection statistic for that search. Over an independent ensemble of similar searches in the presence of stationary Gaussian noise, $2\mathcal{F}^*$ is a random variable that follows a χ^2 distribution with four degrees of freedom. If the data also contain a signal, this distribution has a non-centrality parameter λ proportional to the time-integral of the squared signal.

Detection of that signal would be signified by a large value \mathcal{F}^* unlikely to have arisen from the noise-only distribution. If instead the value is consistent with pure noise (as we find in this instance), we can place an upper limit on the strength of any signal present, as follows:

Let \mathcal{F}^* be the value of the detection statistic in our actual experiment. Had there existed in the data a real signal with amplitude greater than or equal to $h_0(C)$, then in an ensemble of identical experiments with different realizations of the noise, some fraction of trials C

⁵ Note that this detection statistic has nothing to do with the F-statistic of the statistical literature, which is ratio of two sample variances, or the F-test of the null hypothesis that the two samples are drawn from distributions of the same variance.

would yield a detection statistic exceeding the value \mathcal{F}^* . We will therefore say that we have placed an upper limit $h_0(C)$ on the strength of the targeted signal, with confidence C . This is a standard frequentist upper limit.

To determine the probability distribution $p(2\mathcal{F}|h_0)$, we produce a set of simulated artificial signals with fixed amplitude h_0 from fictional pulsars at the position of our target source, and with the same spin-down parameter value, but with intrinsic emission frequencies that differ from it by a few tenths of a hertz. We inject each of these artificial signals into our data and run a search with a perfectly matched template. For each artificial signal we obtain an independent value of the detection statistic; we then histogram these values. If the SFT data in nearby frequency bins (of order 100 bins) can be considered as different realizations of the same random process (justified in IV B), then it is reasonable to assume that the normalized histogram represents the probability density function $p(2\mathcal{F}|h_0)$. One can then compute the confidence

$$C(h_0) = \int_{2\mathcal{F}^*}^{\infty} p(2\mathcal{F}|h_0) d(2\mathcal{F}), \quad (4.5)$$

where $h_0(C)$ is the functional inverse of $C(h_0)$. In practice, the value of the integral in Eq. 4.5 is calculated directly from our simulations as follows: we count how many values of \mathcal{F} are greater or equal to \mathcal{F}^* and divide this number by the total number of \mathcal{F} values. The value derived in this way does not rely on any assumptions about the shape of the probability distribution function (pdf) curve $p(2\mathcal{F}|h_0)$.

There is one more subtlety that must be addressed: all eight signal parameters must be specified for each injected artificial signal. The values of source position and spin-down parameters are known from radio data and are used for these injections. Every injected signal has a different frequency but all such frequencies lie in bins that are close to the expected frequency of the target signal, 1 283.86 Hz. The values ι and ψ are not known, and no attempt has been made in this analysis to give them informative priors based on radio data. However, the value of the non-centrality parameter that determines the $p(2\mathcal{F}|h_0)$ distribution does depend on these values. This means that for a given \mathcal{F}^* , a different confidence level can be assigned for the same signal strength, depending on the choice of ι and ψ .

There are two ways to proceed: either inject a population of signals with different values of ι and ψ , distributed according to the priors on these parameters⁶, or pick a single value for ι and for ψ . In the latter case it is reasonable to choose the most pessimistic orientation and polarization of the pulsar with respect to the detector during the observation time. For fixed signal strength,

this choice results in the lowest confidence level and thus, at fixed confidence, in the most conservative upper limit on the signal strength. We have decided to use in our signal injection the worst-case values for ι (which is always $\pi/2$) and ψ , i.e., the values for which the non-centrality parameter is the smallest.

4. The frequency domain S1 analysis for PSR J1939+2134

Table III summarizes the results of the frequency domain analysis. For every interferometer (column 1) the value of the detection statistic for the search for J1939+2134 is reported: $2\mathcal{F}^*$, shown in column 4. Next to it is the corresponding value of the chance probability:

$$P_0(2\mathcal{F}^*) = \int_{2\mathcal{F}^*}^{\infty} p(2\mathcal{F}|h_0 = 0) d(2\mathcal{F}), \quad (4.6)$$

our estimate of how frequently one would expect to observe the measured value of \mathcal{F}^* or greater in the absence of a signal. The values of $P_0(2\mathcal{F}^*)$ are not significant; we therefore conclude that there is no evidence of a signal and proceed to set an upper limit.

T_{obs} is the length of the live-observation time. h_0^{inject} is the amplitude of the population of injected signals that yielded a 95% confidence. The upper limit $h_0^{95\%}$ differs from h_0^{inject} only by the calibration uncertainty, as explained in Section IV E. C_{meas} is the confidence level derived from the injections of fake signals, and ΔC its estimated uncertainty due to the finite sample size of the simulation.

The quantities in the remaining columns can be used to evaluate how far the reported results are from those that one expects. The results shown are remarkably consistent with what one expects based on the noise and on the injected signal: the confidence levels that we determine differ from the expected ones by less than 2%.

Given a perfectly matched template, the expected non-centrality parameter when a signal $h(t)$ is added to white noise with spectral density S_n is

$$\lambda = \frac{2U}{S_n}, \quad (4.7)$$

where $U = \int_{T_{\text{obs}}} |h(t)|^2 dt$. U can also be computed by feeding the analysis pipeline pure signal and by performing the search with a perfectly matched template⁷ having set $S_n(f) = 1$ s. In Table III we report the values of U_0 , for the worst-case $h(t)$ signals for PSR J1939+2134 as ‘seen’ by the interferometers during their respective observation times and with $h_0 = 2 \times 10^{-19}$. The different values of U_0 reflect the different durations of the

⁶ The time domain analysis assumes uniform priors on $\cos \iota$ and ψ .

⁷ This is indeed one of the consistency checks that have been performed to validate the analysis software. We have verified that the two values of U agree within a 1% accuracy.

IFO	T_{obs} [d]	h_0^{inject}	$2\mathcal{F}^*$	$P_0(2\mathcal{F}^*)$	$\langle 1/S_n \rangle^{-1}$ [Hz $^{-1}$]	$U_0/10^{-33}$ [s]	λ_{exp}	$\lambda_{\text{best-fit}}$	C_{exp}	$C_{\text{best-fit}}$	$C_{\text{meas}} \pm \Delta C$
GEO	16.7	1.94×10^{-21}	1.5	0.83	5.3×10^{-38}	1.0	3.6	3.3	95.7%	95.2%	$95.01 \pm 0.23\%$
L1	5.73	2.70×10^{-22}	3.6	0.46	1.4×10^{-40}	0.37	9.6	8.3	96.7%	95.0%	$95.00 \pm 0.23\%$
H1	8.73	5.37×10^{-22}	6.0	0.20	5.4×10^{-40}	0.5	13.3	12.8	96.6%	95.0%	$95.00 \pm 0.23\%$
H2	8.90	3.97×10^{-22}	3.4	0.49	3.8×10^{-40}	0.45	9.3	7.9	96.8%	95.0%	$95.00 \pm 0.23\%$

TABLE III: Summary of the frequency domain search analyses. T_{obs} indicates the total duration of the analyzed data set. \mathcal{F}^* is the measured value of the detection statistic. $P_0(2\mathcal{F}^*)$ is the probability of getting this value or greater by chance, i.e. in the absence of any signal. h_0^{inject} is the amplitude of the population of fake signals that were injected in the data set such that, when searched for with a perfectly matched template, $C_{\text{meas}}\%$ of the time the resulting value of \mathcal{F} was greater than \mathcal{F}^* . $\langle 1/S_n \rangle$ is the average value of the inverse of the noise in a small frequency band around the target frequency. U_0 is the time integral of the square of the targeted signal with an amplitude of 2×10^{-19} , at the output of the interferometers, for observations times equal to T_{obs} and in the absence of noise. λ_{exp} is the value of the non-centrality parameter that one expects for the distribution of \mathcal{F} from searches with perfectly matched templates on a population of injected signals with amplitude h_0^{inject} and noise with average power $\langle 1/S_n \rangle^{-1}$. $\lambda_{\text{best-fit}}$ is the best-fit non-centrality parameter value derived from the distribution $p(2\mathcal{F}|h_0^{\text{inject}})$ derived from the software signal injections and searches with perfectly matched templates. C_{exp} and $C_{\text{best-fit}}$ are the corresponding confidence values for \mathcal{F}^* .

observations and the different orientations of each detector with respect to the source. The expected value of the non-centrality parameter can be estimated as:

$$\lambda_{\text{exp}} = 2U_0 \langle 1/S_n \rangle \left(\frac{h_0^{\text{inject}}}{2 \times 10^{-19}} \right)^2. \quad (4.8)$$

If the noise were stationary, then S_n may be easily determined. Our noise is not completely stationary, so the value determined for the non-centrality parameter λ is sensitive to the details of how S_n is estimated. The value of $\langle 1/S_n \rangle$ used to determine the expected value of λ is computed as

$$\langle 1/S_n \rangle = \frac{\Delta t}{M} \sum_{\alpha} \frac{1}{\sum_k^M |\tilde{x}_{\alpha k}|^2 / M}, \quad (4.9)$$

Fig. 6 shows the distributions for $p(2\mathcal{F}|h_0^{\text{inject}})$. The circles result from the simulations described above. The solid lines show the best fit non-central χ^2 curves. The shaded region is the integral of $p(2\mathcal{F}|h_0^{\text{inject}})$ between $2\mathcal{F}^*$ and ∞ . By definition this area is 0.95.

D. The time domain search technique

1. Overview

Frequency domain methods offer high search efficiencies when the frequency of the signal and/or the position of the neutron star are unknown and need to be determined along with the other signal parameters. However in the case of known pulsars, where both the intrinsic rotation frequency of the neutron star and its position are known to high accuracy, alternative time domain meth-

ods become attractive. At some level the two domains are of course equivalent, but issues such as data dropouts and the handling of signals with complicated phase evolutions can be conceptually (and practically) more straightforward in a time series analysis than in an analysis based on Fourier transforms.

λ_{exp} is the expected value of the non-centrality parameter based on S_n and h_0^{inject} . $\lambda_{\text{best-fit}}$ is the best-fit value of the non-centrality parameter based on the measured distribution of \mathcal{F} values from the simulation. C_{exp} and $C_{\text{best-fit}}$ are the confidence levels corresponding to these distributions integrated between $2\mathcal{F}^*$ and ∞ .

ods become attractive. At some level the two domains are of course equivalent, but issues such as data dropouts and the handling of signals with complicated phase evolutions can be conceptually (and practically) more straightforward in a time series analysis than in an analysis based on Fourier transforms.

The time domain search technique employed here involves multiplying (heterodyning) the quasi-sinusoidal signal from the pulsar with a unit-amplitude complex function that has a phase evolution equal but of opposite sign to that of the signal. By carefully modelling this expected phase, $\Phi(t)$, we can take account of both the intrinsic frequency and spin-down rate of the neutron star and its Doppler shift. In this way the time-dependence of the signal is reduced to that of the strain antenna pattern, and we are left with a relatively simple model-fitting problem to infer the unknown pulsar parameters h_0 , ι , ψ and ϕ_0 defined in Eqs 3.3 and 3.4.

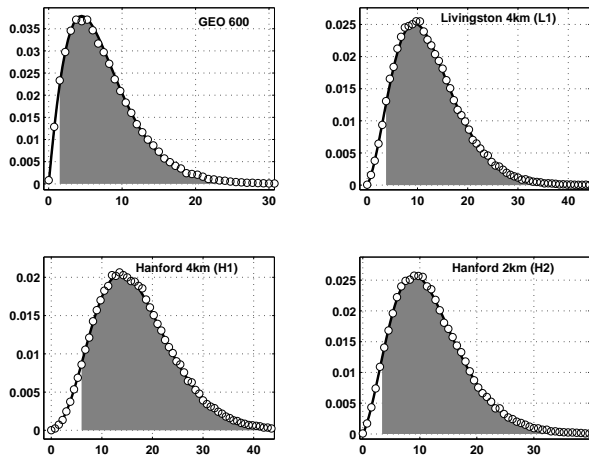


FIG. 6: Measured pdf for $2\mathcal{F}$ for all four interferometer data with injected signals as described in Table III. The circles represent the measured pdf values from the Monte Carlo simulations. The lines represent χ^2 distributions with 4 degrees of freedom and best-fit non centrality parameters given in Table III. The filled area represents the integral of the pdfs between $2\mathcal{F}^*$ and $+\infty$.

In the time domain analysis we take a Bayesian approach and therefore express our results in terms of posterior probability distribution functions for the parameters of interest. Such pdfs are conceptually very different from those used to describe the \mathcal{F} statistic used in the frequency domain search, and represent the distribution of our *degree of belief* in the values of the unknown parameters, based on the experiments and stated prior pdfs.

The time domain search algorithm comprises stages of heterodyning, noise estimation and parameter estimation. In outline, the data are first heterodyned at a constant frequency close to the expected frequency of the signal, low-pass filtered to suppress contamination from strong signals elsewhere in the detector band and re-binned to reduce the sampling frequency from 16 384 Hz to 4 Hz. A second (fine) heterodyne is applied to the data to account for the time-varying Doppler shift and spin-down of the pulsar and any final instrumental calibration, and the data are re-binned to 1 sample per minute. We take the data as stationary during this period, and make an estimate of the noise variance in each 1 min bin from the variance and covariance of the data contributing to that bin. This variance is used in the likelihood function described below.

The parameter estimation stage, at which we set the Bayesian upper limit on h_0 , proceeds from the joint probability of these 1-min complex samples, $\{B_k\}$. We take these B_k values to have a Gaussian likelihood with respect to our signal model, $y(t_k; \mathbf{a})$, where \mathbf{a} is a vector in our parameter space with components $(h_0, \iota, \psi, \phi_0)$ and t_k is the time-stamp of the k th sample. The signal model,

the complex heterodyne of Eq. 3.3, is

$$y(t_k; \mathbf{a}) = \frac{1}{4} F_+(t_k; \psi) h_0 (1 + \cos^2 \iota) e^{i2\phi_0} - \frac{i}{2} F_\times(t_k; \psi) h_0 \cos \iota e^{i2\phi_0}. \quad (4.10)$$

We choose uniform prior probabilities for ϕ_0 over $[0, 2\pi]$ and ψ over $[-\pi/4, \pi/4]$, and a prior for ι that is uniform in $\cos \iota$ over $[-1, 1]$, corresponding to a uniform probability per unit solid angle of pulsar orientation. These uniform priors are uninformative in the sense that they are invariant under changes of origin for the parameters. Although strictly a scale parameter, the prior for h_0 is also chosen as constant for $h_0 \geq 0$, and zero $h_0 < 0$. This is a highly informative prior, in the sense that it states that the prior probability that h_0 lies between 10^{-24} and 10^{-25} is 10 times less than the prior probability it lies between 10^{-23} and 10^{-24} , but guarantees that our posterior pdf can be normalized.

The joint posterior pdf for these parameters is

$$p(\mathbf{a}|\{B_k\}) \propto p(\mathbf{a}) \exp \left[- \sum_k \frac{\Re\{B_k - y(t_k; \mathbf{a})\}^2}{2\sigma_{\Re\{B_k\}}^2} \right] \times \exp \left[- \sum_k \frac{\Im\{B_k - y(t_k; \mathbf{a})\}^2}{2\sigma_{\Im\{B_k\}}^2} \right], \quad (4.11)$$

where $p(\mathbf{a})$ ($\propto \sin \iota$) is the prior on \mathbf{a} , $\sigma_{\Re\{B_k\}}^2$ is the variance of the real parts of B_k , and $\sigma_{\Im\{B_k\}}^2$ is the variance of the imaginary parts of B_k .

The final stage in the analysis is to integrate this posterior pdf over the ι , ψ and ϕ_0 parameters to give a marginalized posterior for h_0 of

$$p(h_0|\{B_k\}) \propto \iiint p(\mathbf{a}|\{B_k\}) d\iota d\psi d\phi_0, \quad (4.12)$$

normalized so that $\int_0^\infty p(h_0|\{B_k\}) dh_0 = 1$. This curve represents the distribution of our degree of belief in any particular value of h_0 , given the model of the pulsar signal, our priors for the pulsar parameters, and the data. The width of the curve roughly indicates the range in values consistent with our state of knowledge.

By definition, given our data and priors, there is a probability of 0.95 that the true value of h_0 lies below $h_0^{95\%}$ where

$$0.95 = \int_0^{h_0^{95\%}} p(h_0|\{B_k\}) dh_0, \quad (4.13)$$

and this defines our 95%-credible Bayesian upper limit on h_0 .

An attraction of this analysis is that data from different detectors can be combined directly using the appropriate signal model for each. The combined posterior distribution from all the available interferometers comes

naturally out of a Bayesian analysis and, for independent observations, is simply the (normalized) product of the contributing probability distributions, i.e.,

$$p(\mathbf{a}|\text{all data}) \propto p(\mathbf{a}|\text{GEO}) \times p(\mathbf{a}|\text{H1}) \times p(\mathbf{a}|\text{H2}) \times p(\mathbf{a}|\text{L1}). \quad (4.14)$$

This posterior pdf embodies all we believe we know about the values of the parameters, optimally combining the data from all the interferometers in a coherent way. For interferometers with very different sensitivities, this will closely approximate the result from the most sensitive instrument. Again, we must marginalize over ι , ψ and ϕ_0 to obtain the posterior pdf for h_0 alone. We note that this is more than simply a combination of the marginalized pdfs from the separate interferometers as the coherence between the instruments is preserved, and it recognizes the different polarization sensitivities of each.

Equipment timing errors discovered after S1 cautioned against a coherent multi-interferometer analysis with this data set. In principle we could assign a suitable prior for the resulting phase offsets and marginalize over them. However, the dominant position of the Livingston 4km interferometer means that even a fully a coherent analysis would only improve our sensitivity by about 20%, so we have not pursued this. Fully coherent analyses will be possible in future observing runs.

2. The time-domain S1 analyses for PSR J1939+2134

The time domain search used contiguous data segments 300s or longer in duration.

The effectiveness of the noise estimation procedure described above was assessed from histograms of $B/\sigma = \Re(B_k)/\sigma_{\Re\{B_k\}} + \Im(B_k)/\sigma_{\Im\{B_k\}}$. If the estimates are correct, and our likelihood function is well modelled by a Gaussian, these histograms (Fig. 7) should also be Gaussian with a variance of one. Since we divide the noise between the real and imaginary components we expect the value of χ^2 to be close (within $\sqrt{2N}$) of the number of real and imaginary data, N (twice the number of complex binned data values B_k). A small number of outliers with magnitudes of B_k/σ_k larger than 5 were not included in this or subsequent analyses.

The marginalized posterior pdfs for h_0 are plotted as the solid lines in Fig. 8. These represent the distribution of our degree of belief in the value of h_0 , following S1, for each interferometer. The width of each curve roughly indicates the range in values consistent with our priors and the data from the instruments individually. The formal 95% upper limits from this analysis are the upper bounds to the shaded regions in the plots, and are 2.2×10^{-21} for GEO, 1.4×10^{-22} for L1, 3.3×10^{-22} for H1, and 2.4×10^{-22} for H2.

The dotted line in the GEO plot of Fig. 8 shows the (very different) marginalized posterior pdf obtained when a simulated signal is added to the data with an amplitude of 2.2×10^{-21} , and with $\phi_0 = 0^\circ$, $\psi = 0^\circ$ and $\iota = 0^\circ$.

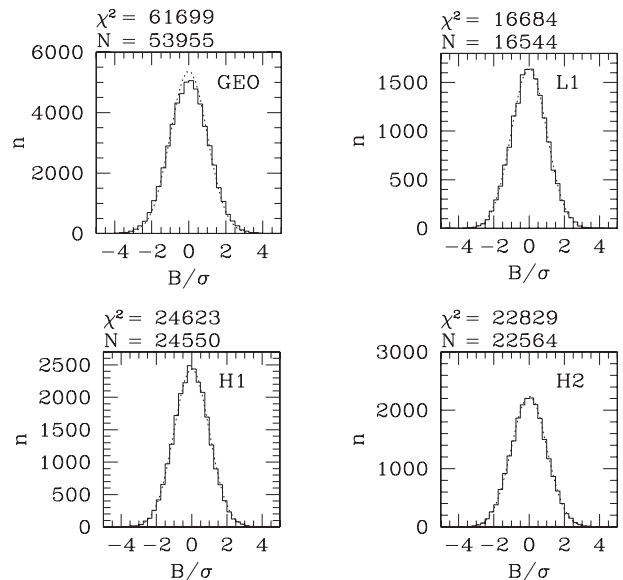


FIG. 7: Histograms of $B/\sigma = \Re(B_k)/\sigma_{\Re\{B_k\}} + \Im(B_k)/\sigma_{\Im\{B_k\}}$ for each interferometer. The dotted lines represent the expected Gaussian distribution, with $\mu = 0$ and $\sigma = 1$.

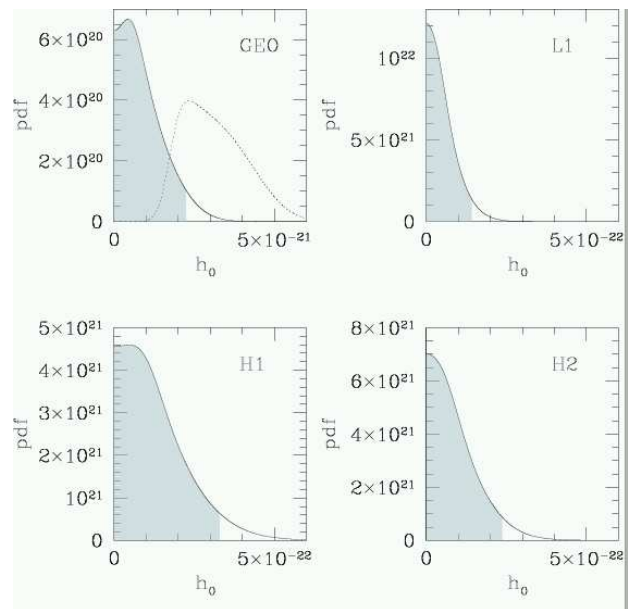


FIG. 8: For each interferometer, the solid line represents the marginalized posterior pdf for h_0 (PSR J1939+2134) resulting from the S1 data. The 95% upper limits (extent of the shaded region) are 2.2×10^{-21} for GEO, 1.4×10^{-22} for L1, 3.3×10^{-22} for H1 and 2.4×10^{-22} for H2. The dotted line in the GEO plot shows the posterior pdf of h_0 in the presence of a simulated signal injected into the GEO S1 data stream using $h_0 = 2.2 \times 10^{-21}$, $\phi_0 = 0^\circ$, $\psi = 0^\circ$ and $\iota = 0^\circ$.

Here there is a clear non-zero lower limit for the value of h_0 , and a result such as this would have indicated a nominal detection, had we seen it.

E. Estimation of uncertainties

In the frequency domain analysis the uncertainty on the upper limit value, $h_0^{95\%}$, has two contributions. The first stems from the uncertainty on the confidence ($\Delta C \approx 0.23\%$) that results from the finite sample size of the simulations. In order to convert this uncertainty into an uncertainty on $h_0^{95\%}$, we have performed several additional Monte Carlo simulations. For every run we have injected a population of signals with a given strength, h_0^{inject} , near $h_0^{95\%}$, searched for each of them with a perfectly matched template and derived a value of \mathcal{F} . With these values we were able to estimate the $h_0(C)$ curve near $h_0^{95\%}$, its slope h'_0 and from this the uncertainty on the value of h_0^{inject} :

$$\Delta h_0^{95\%} \approx h'_0 \Delta C. \quad (4.15)$$

The second contribution to the uncertainty on the value of $h_0^{95\%}$ comes from errors in the calibration of the instruments, which influence the absolute sensitivity scale. In particular this reflects in an uncertainty in the actual value of the strength of injected signals so that $h_0^{95\%} = h_0^{\text{inject}} \pm \delta h_0^{\text{cal}}$. The sum of this error, estimated in II A, and the error arising from the finite sample size, Eq. 4.15, is given in the frequentist results in Table IV.

Note that when a pulsar signal is present in the data, errors in the calibration introduce errors in the phase and amplitude of that signal. The errors in \mathcal{F} due to the signal are quadratic with the errors in the phase and are linear with the errors in the amplitude. However the estimate of the noise spectral density is also affected by calibration errors, and in particular by the amplitude errors. The net effect on \mathcal{F} is that the resulting error on this quantity (which can be considered a sort of signal-to-noise ratio) is quadratic in calibration errors, thus insensitive, to first order, to calibration errors.

The errors quoted for the Bayesian results in Table IV simply reflect the calibration uncertainties given in II A. For clarity, no attempt has been made to fold a prior for this calibration factor into the marginal analysis.

V. CONCLUSION

A. Summary of results

Table IV summarizes the 95% upper limit (UL) results that we have presented in the previous sections. We should stress once more that the two analyses address two well-posed but *different* questions, and the common nomenclature is somewhat misleading.

The frequentist upper limit statements made in Section IV C refer to the likelihood of measuring a given value of the detection statistic or greater in repeated experiments, assuming a value for h_0 and a least-favorable orientation for the pulsar. The Bayesian limits set in Section IV D 1 refer to the cumulative probability of the value of h_0 itself given the data and prior beliefs in the parameter values.

IFO	Frequentist FDS	Bayesian TDS
GEO	$(1.9 \pm 0.1) \times 10^{-21}$	$(2.2 \pm 0.1) \times 10^{-21}$
L1	$(2.7 \pm 0.3) \times 10^{-22}$	$(1.4 \pm 0.1) \times 10^{-22}$
H1	$(5.4 \pm 0.6) \times 10^{-22}$	$(3.3 \pm 0.3) \times 10^{-22}$
H2	$(4.0 \pm 0.5) \times 10^{-22}$	$(2.4 \pm 0.2) \times 10^{-22}$

TABLE IV: Summary of the 95% upper limit values of h_0 for PSR J1939+2134. The frequency domain search (FDS) quotes a conservative frequentist upper limit and the time domain search (TDS) a Bayesian upper limit after marginalizing over the unknown ι , ψ and ϕ_0 parameters.

The Bayesian upper limits report intervals in which we are 95% certain that the true value resides. We do not expect two such distinct definitions of ‘upper limit’ to yield the same numerical value.

Recall that the frequentist UL is *conservative*: it is calculated for the worst-case values of signal parameters ι and ψ . The Bayesian TDS method marginalizes over these parameters, gathering together the evidence supporting a particular h_0 *irrespective of orientation*. We have also performed an alternative calculation of the frequentist ULs by using a $p(\mathcal{F}|h_0)$ derived from a population of signals with $\cos \iota$ and ψ parameters uniformly distributed, as were the Bayesian priors in the time domain search. As expected, we find that the resulting ULs have somewhat lower values than the conservative ones reported in Table IV: 1.2×10^{-21} , 1.5×10^{-22} , 4.5×10^{-22} and 2.3×10^{-22} for the GEO, L1, H1 and H2 data sets respectively.

B. Discussion of previous upper limit results

Two prior upper limits have been published on the strain of a signal from our specific pulsar J1939+2134. A limit of $h < 3.1 \times 10^{-17}$ and 1.5×10^{-17} for the first and second harmonic of the rotation frequency of the pulsar, respectively, was set in [49] using 4 d of data from the Caltech 40 m interferometer. A tighter limit $h < 10^{-20}$ was determined using a divided-bar gravitational wave detector at Glasgow University for the second harmonic alone [44].

More sensitive untargeted UL results on the strain of periodic GW signals at other frequencies come from acoustic bar detector experiments [39], [40] and [42]. Due to the narrow sensitivity bands of these detectors (less than 1 Hz around each mode), and the fact that their frequencies do not correspond to those of any known pulsars⁸, studies with bar antennas have not investigated

⁸ With the exception of the Australian detector NIOBE and of the Japanese torsional antenna built specifically to detect periodic signals from the Crab pulsar [43].

possible emission from any known pulsars.

In [39] a UL of 2.9×10^{-24} was reported for periodic signals from the Galactic center, with $921.32 < f_s < 921.38$ Hz and no appreciable spin-down over ~ 95.7 days of observation. These data were collected by the EXPLORER detector in 1991. This UL result was *not* obtained by a coherent search over the entire observation time, due to insufficient timing accuracy.

In [40] a fully coherent 2 day-long all-sky search was performed again on 1991 EXPLORER data in a f_s search band of about 1 Hz centered at 922 Hz and including 1 spin-down parameter. It resulted in an UL of 2.8×10^{-23} at the 99% confidence level. This search was based on the same detection statistic used in our frequency domain analysis.

Another parameter space search is presented in [42]. Data taken from the ALLEGRO detector during the first three months of 1994 were searched for periodic gravitational wave signals from the Galactic center and from the globular cluster 47 Tuc, with no resolvable spin-down and with f_s in the two sensitive bands of their antenna, 896.30 – 897.30 Hz and 919.76 – 920.76 Hz, with a $10 \mu\text{Hz}$ resolution. The resulting UL at 8×10^{-24} is reported.

There exist several results from searches using early broadband interferometric detectors [44, 45, 46, 47, 48, 49]. Due to the poor sensitivities of these early detector prototypes, none of these upper limits is competitive with the strain sensitivity achieved here. However, many of the new issues and complications associated with broadband search instruments were first confronted in these early papers, laying the foundations for future analyses.

Data from the first science run of the TAMA detector were searched for continuous waves from SN1987A in a 0.05 Hz band at ~ 934.9 Hz. The reported 99% confidence upper limit was $\sim 5 \times 10^{-23}$ [50].

Improved noise performance and longer observation times achieved with interferometric detectors since S1 has made their sensitivities comparable to or better than the narrow band peak sensitivity of the acoustic bars cited above, over much broader bandwidths. Combined with the advances in analysis methods presented in this paper we anticipate significant advances in search depth and breadth in the next set of observations.

C. Upper limit on the ellipticity of the pulsar

An UL on h_0 for J1939+2134 can be interpreted as an UL on the neutron star's equatorial ellipticity. Taking the distance to J1939+2134 to be 3.6 kpc, Eq. 3.1 gives an UL on ellipticity corresponding to $h_0^{95\%} < 1.4 \times 10^{-22}$ of

$$\epsilon^{95\%} = 2.9 \times 10^{-4} \left(\frac{10^{45} \text{ g cm}^2}{I_{zz}} \right). \quad (5.1)$$

Of course, the UL on the ellipticity of J1939+2134 derived from S1 data is about five orders of magnitude higher than the UL obtained from the pulsar's measured

spindown rate: $\epsilon \leq 3.80 \times 10^{-9} (10^{45} \text{ g cm}^2 / I_{zz})^{1/2}$. However, an ellipticity of $\sim 10^{-4}$ could in principle be generated by an interior magnetic field of strength $\sim 10^{16}$ G, or it could probably be sustained in a NS with a solid core. Therefore, the above exercise suggests that with improved detector sensitivities, even a null result from a search for *unknown* pulsars will place interesting constraints on the ellipticities of rapidly-rotating neutron stars that might exist in our galactic neighborhood.

VI. ACKNOWLEDGEMENTS

The authors gratefully acknowledge the support of the United States National Science Foundation for the construction and operation of the LIGO Laboratory and the Particle Physics and Astronomy Research Council of the United Kingdom, the Max-Planck-Society and the State of Niedersachsen/Germany for support of the construction and operation of the GEO600 detector. The authors also gratefully acknowledge the support of the research by these agencies and by the Australian Research Council, the Natural Sciences and Engineering Research Council of Canada, the Council of Scientific and Industrial Research of India, the Department of Science and Technology of India, the Spanish Ministerio de Ciencia y Tecnologia, the John Simon Guggenheim Foundation, the David and Lucile Packard Foundation, the Research Corporation, and the Alfred P. Sloan Foundation.

- [1] The LIGO Scientific Collaboration, “Detector description and performance for the First Coincidence Observations between LIGO and GEO”, in preparation, (2003).
- [2] A. Abramovici et al., *Science* **256**, 325 (1992).
- [3] B. Barish and R. Weiss, *Phys. Today* **52**, 44 (1999).
- [4] B. Willke et al., *Class. Quant. Grav.*, **19(7)**, 1377 (2002).
- [5] S. Goßler et al., *Class. Quant. Grav.*, **19(7)**, 1835 (2002).
- [6] A. Einstein, *Die Feldgleichungen der Gravitation*, Preuss. Akad. Wiss. Berlin, Sitzber, 844-847 (publ. Dec 2, 1915).
- [7] A. Einstein, *Naeherungsweise Integration der Feldgleichungen der Gravitation*, Preuss. Akad. Wiss. Berlin, Sitzber, 688-696 (1916).
- [8] B. Caron et al., *Nucl. Phys. B-Proc. Suppl.*, **54**, 167 (1997).
- [9] K. Tsubono, in *1st Edoardo Amaldi Conf. Gravitational Wave Experiments* edited by E. Coccia, G. Pizzella, and F. Ronga (World Scientific, Singapore, 1995), p. 112.
- [10] B. Allen, M.A. Papa, and B.F. Schutz, *Phys. Rev. D* **66**, 102003 (2002).
- [11] P. Jaranowski, A. Królak, and B.F. Schutz, *Phys. Rev. D* **58**, 063001 (1998).
- [12] P.R. Brady, T. Creighton, C. Cutler, and B.F. Schutz, *Phys. Rev. D* **57**, 2101 (1998).
- [13] P. Fritschel, *Proceedings of SPIE Volume 4856, Gravitational Wave Detection, Waikoloa, HI*, **4856**, 39 (2002).
- [14] L. Bildsten, *Astrophys. J.* **501**, L89 (1998).
- [15] L. Bildsten, astro-ph/0212004 to appear in *Radio Pulsars* edited by M. Bailes, D.J. Nice, and S.E. Thorsett (ASP Conference Series).
- [16] D. Chakrabarty, E.H. Morgan, M.P. Muno, D.G. Galloway, R. Wijnands, M. van der Klis, C. Markwardt, *Nature*, **424**, 42 (2003).
- [17] R. Wijnands, M. van der Klis, J. Homan, D. Chakrabarty, C.B. Markwardt, E.H. Morgan, *Nature* **424**, 44 (2003).
- [18] R.V. Wagoner, *Astrophys. J.* **278**, 345 (1984).
- [19] R.V. Wagoner, *Nature* **424**, 27 (2003).
- [20] F. Verbunt, *Annual Review of Astronomy and Astrophysics*, **31**, 93 (1993).
- [21] M. van der Klis, *Annual Review of Astronomy and Astrophysics*, **38**, 717 (2000).
- [22] D.I. Jones and N. Andersson, *Mon. Not. R. Astron. Soc.* **331**, 203 (2002).
- [23] R. Jenet and S.B. Anderson, *Astrophys. J.* **546**, 394 (2001).
- [24] A.N. Lommen and D.C. Backer, pers. comm.
- [25] N. Andersson, *Astrophys. J.* **502**, 708 (1998).
- [26] J.L. Friedman and S.M. Morsink, *Astrophys. J.* **502**, 714 (1998).
- [27] P. Arras, E.E. Flanagan, S.M. Morsink, A.K. Schenk, S.A. Teukolsky, and I. Wasserman, astro-ph/0202345.
- [28] G. Ushomirsky, C. Cutler, and L. Bildsten, *Mon. Not. R. Astron. Soc.* **319**, 902 (2000).
- [29] C. Cutler, *Phys. Rev. D* **66**, 084025 (2002).
- [30] J.H. Taylor, *Phil. Trans. R. Soc. Lon. A* **341**, 117 (1992).
- [31] <http://pulsar.princeton.edu/tempo/index.html>.
- [32] A. O’Hagan *Kendall’s Advanced Theory of Statistic*, Halsted Press, **2B: Bayesian Inference** (1994).
- [33] L.S. Finn, in *Second Edoardo Amaldi Conference on Gravitational Waves* edited by E. Coccia, G. Veneziano, G. Pizzella (World Scientific), 180 (1998).
- [34] V.M. Kaspi, J.H. Taylor and M.F. Ryba, *Astrophys. J.* **428**, 713 (1994).
- [35] <http://www.lsc-group.phys.uwm.edu/lal/>.
- [36] <http://www.cs.wisc.edu/condor/> “Condor is a specialized workload management system for compute-intensive jobs. Like other full-featured batch systems, Condor provides a job queueing mechanism, scheduling policy, priority scheme, resource monitoring, and resource management. Users submit their serial or parallel jobs to Condor, Condor places them into a queue, chooses when and where to run the jobs based upon a policy, carefully monitors their progress, and ultimately informs the user upon completion.”
- [37] <http://www.lsc-group.phys.uwm.edu/beowulf/medusa/index.html>
- [38] <http://pandora.aei.mpg.de/merlin>
- [39] P. Astone et al., *Phys. Rev. D* **65**, 022001 (2002).
- [40] P. Astone, K.M. Borkowski, P. Jaranowski, A. Królak, *Phys. Rev. D* **65**, 042003 (2002).
- [41] J. M. Lattimer, in *The Structure and Evolution of Neutron Stars* edited by D. Pines, R. Tagamaki, S. Tsuruta (Addison-Wesley), 50 (1992).
- [42] E. Mauceli, M.P. McHugh, W.O. Hamilton, W.W. Johnson, and A. Morse, gr-qc/0007023.
- [43] T. Suzuki, in *Gravitational Wave Experiments*, edited by E. Coccia, G. Pizzella and F. Ronga (World Scientific), 115 (1995).
- [44] J. Hough et al., *Nature*, **303**, 216 (1983).
- [45] J. Livas, in *Gravitational Wave Data Analysis*, edited by Schutz, (NATO ASI Series C) **253**, 217 (1988) and J. Livas, “Upper limits for gravitational radiation from some astrophysical sources,” Ph.D. dissertation, Massachusetts Institute of Technology (1987).
- [46] T.M. Niebauer et al., *Phys. Rev. D* **47**, 3106 (1993).
- [47] G. S. Jones, “Search for continuous Gravitational Wave sources,” Ph.D. dissertation, University of Wales (Cardiff University), (1995).
- [48] M. Zucker, “Experiments with a laser interferometric gravitational wave antenna,” Ph.D. dissertation, California Institute of Technology (1988).
- [49] M. Hereld, “A search for gravitational radiation from PSR 1937+214,” Ph.D. dissertation, California Institute of Technology (June, 1983).
- [50] K. Soida, M. Ando, N. Kanda, H. Tagoshi, D. Tatsumi, K. Tsubono and the TAMA Collaboration, *Class. Quantum Grav.* **20**, S645 (2003).